ELECTROCHEMISTRY

Identification of the active triple-phase boundary of a non-Pt catalyst layer in fuel cells

Yu-Cheng Wang[1,2]*†, Wen Huang[1]†, Li-Yang Wan[1]†, Jian Yang[1]†, Rong-Jie Xie[1], Yan-Ping Zheng[1], Yuan-Zhi Tan[1], Yue-Sheng Wang[3], Karim Zaghib[4], Li-Rong Zheng[5], Shu-Hui Sun[6]*, Zhi-You Zhou[1,2]*, Shi-Gang Sun[1]

The rational design of non-Pt oxygen reduction reaction (ORR) catalysts and catalyst layers in fuel cells is largely impeded by insufficient knowledge of triple-phase boundaries (TPBs) in the micropore and mesopore ranges. Here, we developed a size-sensitive molecular probe method to resolve the TPB of Fe/N/C catalyst layers in these size ranges. More than 70% of the ORR activity was found to be contributed by the 0.8- to 2.0-nanometer micropores of Fe/N/C catalysts, even at a low micropore area fraction of 29%. Acid-alkaline interactions at the catalyst-polyelectrolyte interface deactivate the active sites in mesopores and macropores, resulting in inactive TPBs, leaving micropores without the interaction as the active TPBs. The concept of active and inactive TPBs provides a previously unidentified design principle for non-Pt catalyst and catalyst layers in fuel cells.

INTRODUCTION

Proton exchange membrane fuel cells (PEMFCs) are clean and efficient electrochemical energy devices, but their commercialization has been severely impeded by the high expense and scarcity of Pt catalysts. Pyrolyzed transition metal/nitrogen/carbon (M/N/C) materials, especially Fe/N/C, have been shown to be the most promising nonprecious metal catalysts to replace Pt for use in PEMFCs to catalyze the cathodic oxygen reduction reaction (ORR) (*1*, *2*). Through active site structure probing (*3*, *4*) and material innovation (*5*–*7*), the intrinsic activity of previously developed Fe/N/C catalysts, which has mostly been tested in aqueous rotating disk electrodes (RDEs), has been greatly improved and has even approached that of Pt in some cases. However, there exists a large gap between aqueous electrode tests and fuel cells, mainly originating from the considerable differences in reaction interfaces (*8*, *9*). In the aqueous RDE test, the ORR takes place at the solid-liquid two-phase interface. Conversely, in fuel cells, the reactions mainly take place at the triple-phase boundary (TPB), where the electrocatalyst, electrolyte, and reactant gas come into contact. For this reason, many ORR catalysts that perform well in aqueous RDE tests do not show high working performance in fuel cells (*10*). In addition, to prevent electrolyte leaching, perfluorosulfonic acid polyelectrolytes (e.g., Nafion) are used in PEMFCs (*11*). Unlike that of the free acids (e.g., H_2SO_4 or $HClO_4$) that are in aqueous tests, the sulfonic anion is fixed on the polymer backbone, and only H^+ can migrate (*12*, *13*). The single-ion mobility and large molecular size of Nafion make the TPB very complex, especially for heterogenetic Fe/N/C catalysts with atomically dispersed active sites in porous structures.

To achieve high fuel cell performance, it is critical to construct a sufficiently efficient TPB. However, the rational construction of such a TPB is mainly impeded by insufficient knowledge of the TPB structure. First, recent studies of TPB in fuel cell catalyst layers have mainly relied on x-ray nanocomputed tomography (*14*, *15*), x-ray scattering tomography (*16*, *17*), helium ion microscopy (*18*), and focused ion beam scanning electron microscopy (SEM) (*19*). These advanced characterization methods can be used to image catalyst-electrolyte interfaces, which reflect the number and distribution of TPBs (*20*, *21*). However, the spatial resolutions of these methods are tens of nanometers (*22*), which is not sufficient to resolve interface information in micropores (<2 nm) and mesopores (2 to 50 nm). Second, recent studies of TPBs have rarely considered catalyst-electrolyte interfacial interactions. These interactions are a determining factor that governs the efficiency of the TPBs. If a strong catalyst-electrolyte interfacial interaction exists that can deactivate active sites, then the typical TPB will no longer be efficient for electrochemical reactions. Coincidentally, pyrolyzed Fe/N/C catalysts inevitably contain some alkaline sites, such as pyridinic N species, which may be protonated by the H^+ in Nafion (*23*). Ignoring these acid-alkaline interfacial interactions may result in an inaccurate understanding of the TPB in the Fe/N/C catalyst layer and consequently incorrect guidance on the design of catalysts and catalyst layers.

Molecular probe methods have important advantages in terms of selectivity and specificity and are suitable for in situ studies of complex systems. However, these methods were previously used only to identify the structures of active sites of M/N/C catalysts in aqueous solutions (*24*). Here, we developed a size-sensitive molecular probe method to reveal effective TPBs and interface interactions in an Fe/N/C catalyst layer in the micropore and mesopore ranges under fuel cell working conditions and gained a previously unidentified insight into the structural design of catalysts and catalyst layers. We found that the TPB formed in micropores between 0.8 and 2.0 nm contributes more than 70% of the ORR activity, although the fraction of the micropore area is as low as 29%. This observation contradicts the previous general hypothesis that ORR active sites in mesopores or macropores are more efficient than micropores because of fast mass

[1]State Key Laboratory of Physical Chemistry of Solid Surfaces, College of Chemistry and Chemical Engineering, Xiamen University, Xiamen 361005, China. [2]Innovation Laboratory for Sciences and Technologies of Energy Materials of Fujian Province (IKKEM), Xiamen 361005, China. [3]Center of Excellence in Transportation Electrification and Energy Storage, Hydro-Québec, Varennes, QC, J3X 1S1, Canada. [4]Department of Mining and Materials Engineering, McGill University, Montréal, QC H3A 0C5, Canada. [5]Beijing Synchrotron Radiation Facility, Institute of High Energy Physics, Chinese Academy of Sciences, Beijing 100049, China. [6]Institut National de la Recherche Scientifique (INRS), Centre Énergie Matériaux Télécommunications, Varennes, QC, J3X 1P7, Canada.
*Corresponding author. Email: wangyc@xmu.edu.cn (Y.-C.W.); shuhui.sun@inrs.ca (S.-H.S.); zhouzy@xmu.edu.cn (Z.-Y.Z.)
†These authors contributed equally to this work.

transfer and ease of formation of the TPB (*25*, *26*). This discrepancy originates from an acid-alkaline interaction of the catalyst-electrolyte interface, i.e., protonation of pyridinic N species in Fe/N/C by Nafion, which deactivates the active sites in mesopores or macropores, resulting in an inactive TPB. This interaction is absent in micropores due to the large size of Nafion, ensuring high catalytic activity and consequently an active TPB.

RESULTS AND DISCUSSION

The Fe/N/C catalyst used in this work was prepared from poly-*m*-phenylenedimaine by a two-step pyrolysis under an Ar atmosphere and was termed PDA-Ar (*24*). The catalyst exhibited high ORR activity and a repeatable current density of 130 to 137 mA cm^{-2} at 0.8 $V_{iR\text{-free}}$ (after correction for ohmic loss R) at kinetic region in H_2-O_2 PEMFC (fig. S1). Consistent with most active M/N/C catalysts (*27*–*30*), the PDA-Ar catalyst was a typical microporous material with a micropore area and an external surface area (pore size: >2 nm) of 418 and 339 $m^2\ g^{-1}$, respectively (fig. S2). To evaluate the ORR activity contribution of pores of different sizes, we developed an electrochemical molecular probe method. As shown in Fig. 1A, organic compounds of different sizes (benzene, naphthalene, pyrene, perchloronaphthalene, tetraphenylporphyrin, $C_{60}Cl_{22}$, and $C_{96}Cl_{27}H_3$, labeled as Ph, Ph_2, Ph_4, $C_{10}Cl_8$, Ph_4Pp, $C_{60}Cl_{22}$, and $C_{96}Cl_{27}$, respectively) were selected as probe molecules. These chemically inert molecules do not react with the PDA-Ar catalyst, as evidenced by the unchanged background cyclic voltammetry (CV) peak after probe molecules were applied (fig. S3). However, they can be physically absorbed by the micropores or external surface of the catalyst. To exclude the pH interference, we conducted absorption before addition of acidic Nafion electrolyte. Physical absorbing molecules on the external surface are not expected to poison the catalytic sites. However, the organic compounds can block a fraction of micropores and impede the transport of reactants (mainly O_2, because its dynamic diameter is larger than those of H^+ and H_2O) (*31*). The largest size (d_p) of pores that can be blocked by organic compounds is reasonably assumed to be the sum of the dynamic diameters of the organic compounds (d_1) and O_2 (d_2), that is, $d_p = d_1 + d_2$. When the pore size is larger than d_p, the gap between the pore wall and the organic compounds is still large enough for reactants to access. Therefore, absorption cannot considerably decrease the fuel cell performance in the kinetic region, i.e., 0.8 V, where the mass transfer is not a limiting factor. By investigating the response of the PDA-Ar cathode toward organic compounds of different sizes, the contribution to ORR activity by pores of different sizes can be differentiated.

For the fuel cell activity test, the catalyst surface coverage by the organics should be kept constant because it can affect the fuel cell activity. The same surface coverage was achieved by optimizing the starting organics concentration for absorption. Figure S4 plots the curve of catalyst coverage area versus the starting organics concentration for the PDA-Ar catalyst. The organics are taken as a sphere, whose diameter is approximate to the dynamic diameter. The catalyst coverage area is determined by accumulating the projected area of the sphere and controlled at 93 $m^2\ g_{cat}^{-1}$ with <4% of deviation for each absorption molecule (Fig. 1B). The size-dependent organics distribution was verified by measuring the Ar isothermal adsorption/desorption. The test was conducted after the organics were applied to the catalyst surface but before the catalyst was fabricated into the membrane electrode assembly (MEA). The Ph and Ph_4Pp decreased the micropore accessibility while affecting little on the mesopore or macropore region (fig. S5). The larger Ph_4Pp blocked more micropore than the smaller Ph even at the same catalyst surface coverage. By contrast, the largest $C_{96}Cl_{27}$ was mainly absorbed by the external surfaces and affected little on the micropore accessibility. This experimental observation is in good agreement with the assumption of size-selective pore blocking.

After clarifying these points, the fuel cell activity test was conducted, as shown in Fig. 1C. The current density at 0.8 $V_{iR\text{-free}}$ of these samples relative to those of organic-free samples are shown in Fig. 1D. The ORR performance was dominated by the molecular size of the organic compounds. After the addition of Ph, only 9.0% of the ORR activity at 0.8 $V_{iR\text{-free}}$ was lost relative to that of the bare sample. Ph can block active sites in pores smaller than 0.8 nm ($d_p \approx$ 0.8 nm; table S1). The observed activity loss suggests that pores smaller than 0.8 nm contribute, at most, 9.0% to the ORR activity. As the size of the organic molecules increases, the ORR activity of the PDA-Ar catalyst decreases. At a critical size of organic compounds, corresponding to Ph_4Pp ($d_p \approx$ 2.0 nm), the current density at 0.8 $V_{iR\text{-free}}$ decreased by 86.3%. This result suggests that pores between 0.8 and 2.0 nm contribute 77.3% to the ORR activity. Larger probe molecules, e.g., $C_{60}Cl_{22}$ ($d_p \approx$ 2.4 nm) and $C_{96}Cl_{27}$ ($d_p \approx$ 3.0 nm), are too large to enter micropores; they are mainly absorbed on the external surfaces of the PDA-Ar catalyst. Correspondingly, less than 10% of the ORR activity was lost, supporting our expectation that physically absorbing molecules on the external surface do not poison the catalytic sites and have little impact on the intrinsic ORR activity. By means of the molecular probe experiment, the contribution of pores of different sizes to the ORR activity can be evaluated, as shown in Fig. 1E, and the efficient pore size was determined to be 0.8 to 2.0 nm for the PDA-Ar catalyst.

To further strengthen the reliability of the molecular probe method and as-derived conclusion, we conducted several exclusion experiments. The factors that are relevant to the fuel cell activity were examined, e.g., the thickness and surface wettability of the catalyst layer and the conductivity of the MEA, so as to verify that the decrease in performance is actually caused by size-dependent pore blocking rather than other factors. The wettability of the catalyst layer was compared by measuring the surface contact angle (fig. S6). The change in the cathode thickness was determined by comparing the cross section using SEM (fig. S7). The proton transport resistance (R_{H+}) of the MEA was measured by electrochemical impedance spectroscopy (fig. S8), and data analysis and fitting were according to a previously reported method of the transmission line mode in an H_2/N_2 atmosphere (*32*, *33*). It was observed that the thickness and wettability of the catalyst layer as well as the conductivity of the MEA are not changed by the addition of organics, further supporting the notion that the size-dependent pore blocking dominates the fuel cell activity loss.

The PDA-Ar catalyst is a typical microporous material. To demonstrate the universality of the probe method and determine efficient pore size ranges for the ORR, we prepared five Fe/N/C catalysts with different pore structures by altering the synthetic process. The synthetic process of PDA-CO_2 series catalysts was similar to that of the PDA-Ar catalyst, except that a CO_2-Ar mixture (1.25, 7, 8.5, and 10% CO_2, respectively) was used instead of pure Ar in the first pyrolysis step (*34*). CO_2 can etch carbon under high temperatures ($CO_2 + C \rightarrow 2CO$) to create more pores. To date, the most active Fe/N/C catalysts have been derived from zeolitic imidazolate frameworks (ZIFs) (*35*–*37*). Therefore, a ZIF-Ar catalyst was prepared by

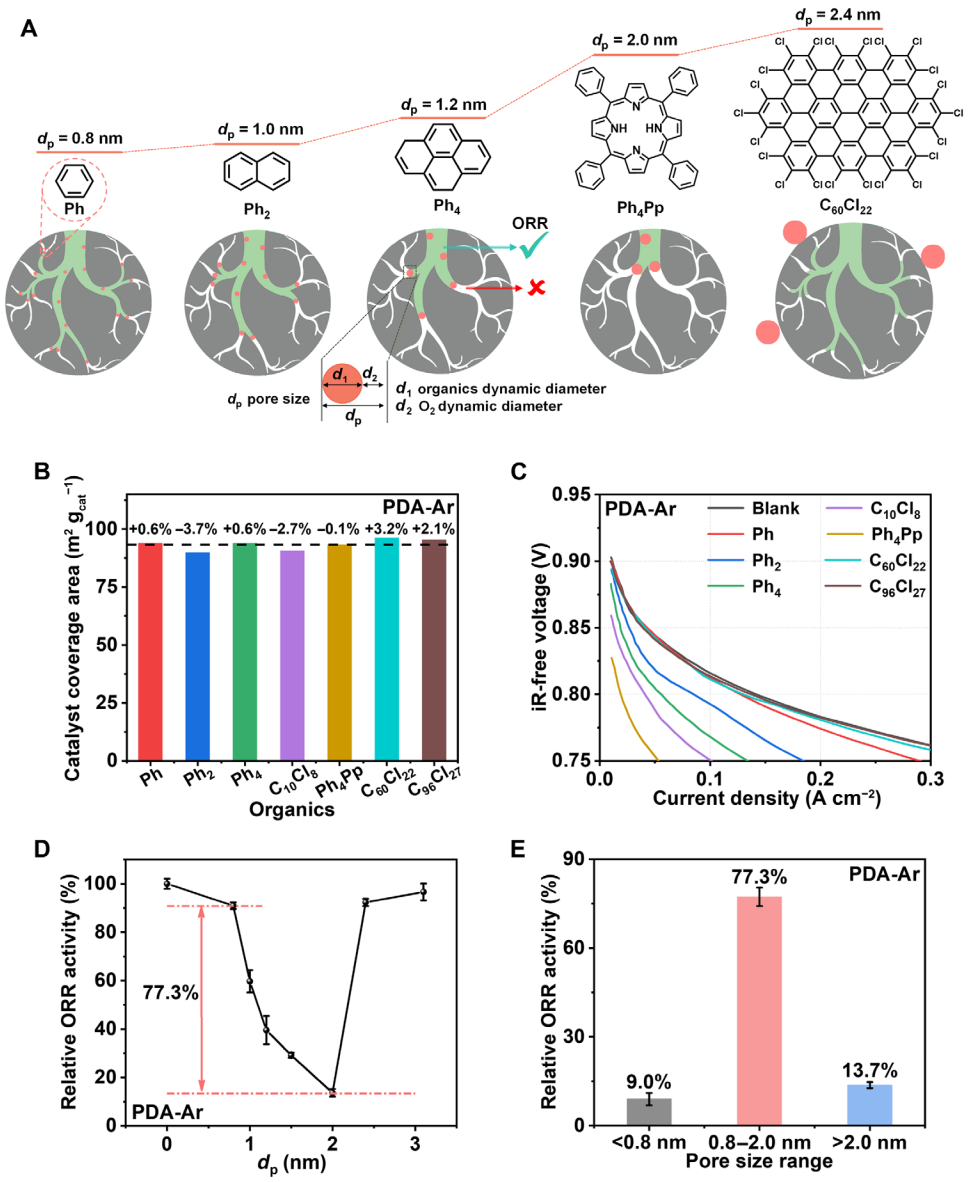

Fig. 1. Electrochemical molecular probe method to identify efficient TPB region. (**A**) A schematic of electrochemical molecular probe method with different-sized organics as probe molecules to determine the ORR contribution from different pore size ranges. (**B**) The controlled coverage area of the PDA-Ar catalyst by seven different-sized organics for the fuel cell activity test. (**C**) Polarization curves (iR-free) of H_2-O_2 PEMFC using the PDA-Ar Fe/N/C as the cathode catalyst with and without the addition of organics. Test conditions are composed of the following: 80°C (cell temperature), 1-bar backpressure, 0.3 SLPM with 100% RH for H_2 and O_2, Nafion 212 membrane, Fe/N/C catalyst with 4.0 mg cm^{-2} (cathode), and Pt/C (40 wt %; JM) with 0.4 mg_{pt} cm^{-2} (anode). (**D**) Relative current density at 0.8 $V_{iR\text{-}free}$ of the PDA-Ar Fe/N/C cathode after the addition of different-sized organics. (**E**) ORR activity contribution from different regions.

a one-step pyrolysis of Fe-doped ZIF-8 particles under an Ar atmosphere (*38*). Figure 2A shows the Ar absorption-desorption isotherms of the six Fe/N/C catalysts, including the PDA-Ar catalyst. Table S2 lists the micropores and external surface area of the six catalysts. Their micropore surface fraction is shown in Fig. 2B and follows the order ZIF-Ar (62%) > PDA-Ar (55%) > PDA–1.25% CO_2 (47%) > PDA–7% CO_2 (36%) > PDA–8.5% CO_2 (33%) > PDA–10% CO_2 (29%), ranging from microporous type to hierarchically porous type. The five PDA series catalysts showed similar carbon morphology and consisted of roughly 100-nm aggregated particles, which is different from the ZIF-Ar consisting of polyhedral carbon structures (fig. S9). The Fe loading of the six catalysts was given by inductively coupled plasma mass spectrometry (ICP-MS), as shown in table S3. The five PDA series catalysts showed a low Fe content of no more than 0.78 weight (wt) %. The combination of x-ray absorption spectroscopy (XAS; fig. S10) and x-ray diffraction (fig S11) confirmed the atomically dispersed Fe species in the five PDA series catalysts. By contrast, the ZIF-Ar exhibited a high Fe content of up to 4.22 wt %, which was attributed to the formation of Fe_3C particles. Among them, the three catalysts, i.e., PDA–7% CO_2, PDA–8.5% CO_2, and PDA–10% CO_2, can be regarded as a group of near model catalysts. They exhibited the same Fe status and the high similarity in Fe content

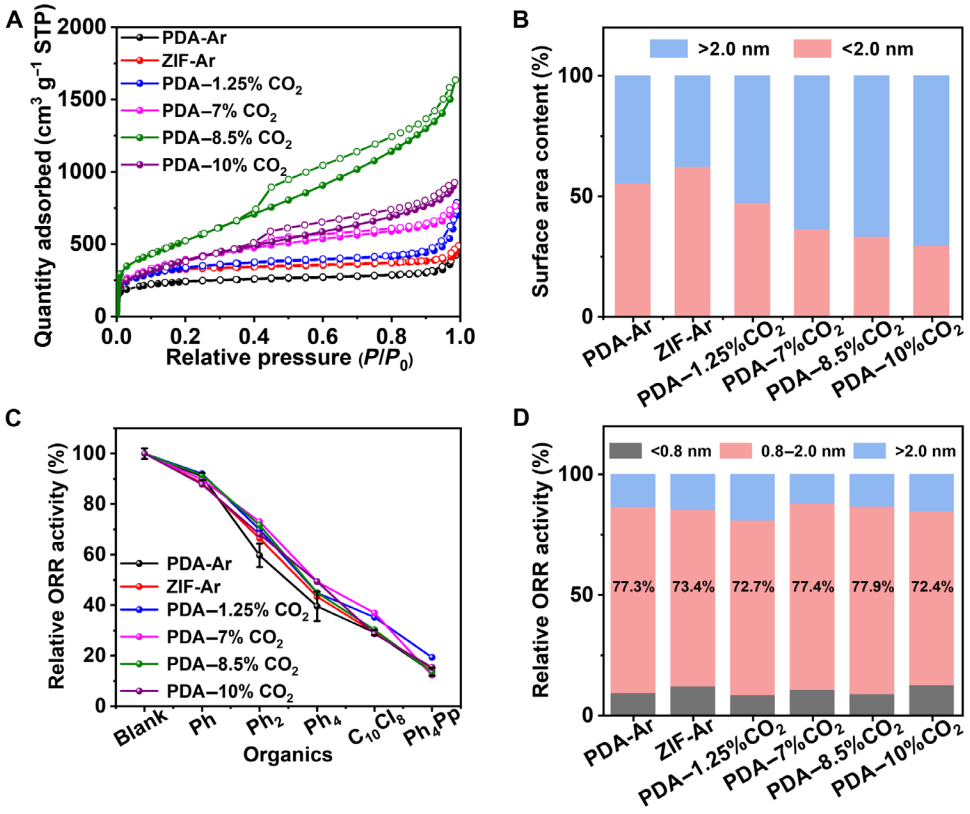

Fig. 2. Universal responses to organics for different Fe/N/C catalysts. (**A**) Ar absorption/desorption isotherm and (**B**) the corresponding micropores (<2 nm) and external surface area (>2 nm) fraction of six Fe/N/C catalysts prepared using different synthetic conditions (*t*-plot method). (**C**) The responses of the six Fe/N/C catalysts toward different-sized organics evaluated by the relative current density at 0.8 $V_{iR\text{-free}}$. (**D**) ORR activity contribution from different-sized porosity for the six Fe/N/C catalysts.

(<15% of the variation), carbon morphology (fig. S12), carbon defect degree (fig. S13), and surface wettability (fig. S14). Therefore, the six Fe/N/C catalysts not only contain three rigorous near-model comparison samples but also show catalyst diversity. If the probe method can be applied to the six Fe/N/C catalysts, then the reliability and universality of as-derived conclusion will be strengthened.

Similar to the PDA-Ar case, the plots of catalyst coverage area versus starting organics concentration were plotted for the five catalysts (fig. S15). For a specific Fe/N/C catalyst, the catalyst coverage area remained constant for different-sized organics (fig. S16). Then, the electrochemical molecular probe experiment was conducted (fig. S17). As shown in Fig. 2C, the five Fe/N/C catalysts showed a similar molecular size–dependent activity change trend to the PDA-Ar catalyst. This similarity supports that the 0.8- to 2.0-nm micropores contribute most to the ORR activity, >70% (Fig. 2D), for the six Fe/N/C catalysts, regardless of their micropore surface fraction (Fig. 2B) and pore distributions (fig. S18).

In general, active sites in mesopores or macropores are considered more efficient than those in micropores for the ORR (*25*), because the former allows fast mass transfer and facile formation of the TPB via Nafion agglomeration (*39*). However, active sites in micropores with sizes from 0.8 to 2.0 nm contribute more than 70% to the ORR activity in PEMFC, even for the Fe/N/C catalyst PDA–10% CO_2 with a micropore surface fraction of only approximately 29%. This finding is unexpected and needs to be clarified.

The cathode catalyst layer consists of an Fe/N/C catalyst and a polymer electrolyte (i.e., Nafion). Nafion, composed of a fluoropolymer backbone with sulfonic acid side chains, exists in the form of clusters in solution, with aggregation sizes of approximately 4 nm (*13*, *40*). The sulfonic acid in Nafion can protonate pyridinic N species (logarithmic acid dissociation constant K_a, $pK_a = 5.4$; fig. S19) in the mesopores and macropores of the Fe/N/C catalyst but cannot easily neutralize those basic species in micropores (Fig. 3A). This conclusion is supported by the negative correlation between the micropore surface fraction and the protonation degree of pyridinic N species (fig. S20 and table S4). Specifically, for a typical microporous catalyst, 71% of pyridinic N exists in an unprotonated state in the presence of Nafion. For hierarchically porous catalysts (e.g., PDA–10% CO_2), almost 100% of pyridinic N is protonated on the near surface where mesopores or macropores dominate, as detected by x-ray photoelectron spectroscopy (XPS), where the band with a binding energy of approximately 402 eV is assigned to protonated pyridinic N (Py-NH^+, Fig. 3B) (*23*, *41*). In the interior, where micropores dominate, 95% of pyridinic N still remains in the unprotonated state (398.5 eV), as detected by XPS after Ar ion etching at approximately 50 nm.

To demonstrate the absence of acid-alkaline interface interactions in micropores resulting in high ORR activity, we selected small H_2SO_4 as a probe molecule. Unlike large Nafion, H_2SO_4 can easily enter micropores and protonate pyridinic N species. Figure 3C shows the polarization curves of the PDA–10% CO_2 cathode with and without

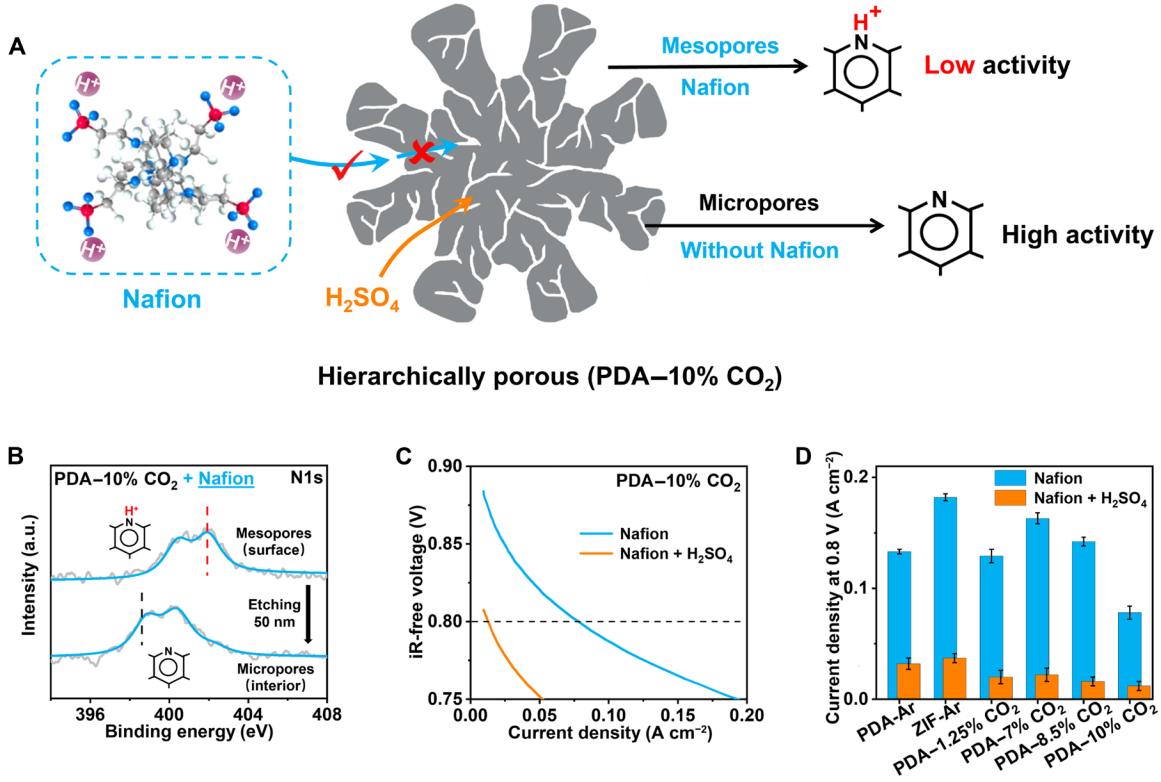

Fig. 3. Effects of acid-alkaline interfacial interactions in micropores and mesopores. (**A**) Schematic of protonation by different-sized acids in hierarchically porous PDA–10% CO_2 catalyst. (**B**) High-resolution N1s XPS in the outer and interior layer of PDA–10% CO_2 catalyst after mixing with Nafion. a.u., arbitrary units. (**C**) Polarization curves of H_2-O_2 PEMFC with PDA–10% CO_2 as the cathode catalyst before and after the addition of H_2SO_4 (1.0 μmol mg_{cat}^{-a}). (**D**) The responses of six Fe/N/C catalysts toward H_2SO_4, evaluated by relative current density at 0.8 $V_{iR\text{-free}}$.

H_2SO_4 treatment (1.0 μmol mg_{cat}^{-1}). In the presence of Nafion alone, the cathode showed a current density of 0.078 A cm^{-2} at 0.8 $V_{iR\text{-free}}$. After H_2SO_4 treatment, the current density at 0.8 $V_{iR\text{-free}}$ decreased by 85%, which may be attributed to protonation of the micropores by H_2SO_4. A similar degree of ORR activity loss after treatment with H_2SO_4 was also observed for nine other Fe/N/C catalysts (Fig. 3D and fig. S21). These observations suggest that the ORR activity in the Fe/N/C cathode is mainly attributed to the micropores, where the acid-alkaline interaction of the catalyst-electrolyte interface is absent.

To clarify the deactivation mechanism of protonation, we conducted a series of physical characterizations and control experiments. Both H_2SO_4 and $HClO_4$ treatments resulted in an ORR activity loss greater than 70% (fig. S22), excluding the specific adsorption of SO_4^{2-} on active sites. Mössbauer (fig. S23 and table S5) and XAS analyses (fig. S9) revealed that acid treatments have little impact on the coordination structure and number of Fe-N_x active sites, excluding the possibility that the acids destroy the active sites. Therefore, an indirect deactivation mechanism was proposed: The protonation of pyridinic N decreases the catalytic efficiency of adjacent Fe-N_x active sites. Such a mechanism was supported by the following experimental evidence: (i) The neutralization of Py-NH^+ to pyridinic N by alkaline treatment led to a 60% recovery of the ORR activity (fig. S24), and (ii) molecular iron phthalocyanine (FePc) with FeN_4 active site but without pyridinic N showed an activity loss of 24% after acid treatment versus 75% loss for the PDA-Ar catalyst (fig. S25). The deactivation phenomenon of Fe/N/C catalysts by protonation has been observed by several groups, but the mechanism is still under debate. Changing the electronic structure of the catalyst by the protonation of pyridinic N (*42*) and incorporating anions with Py-NH^+ cations to suppress the ORR (*43*) have been proposed. To better understand the deactivation mechanism of Py-NH^+ on adjacent Fe-N_x active sites, density functional theory calculations were carried out. Two types of Fe-N-C moieties (C_{35}-FeN_4-N and C_{73}-FeN_4-N) with different pyridinic N sites were constructed to simulate the ORR processes (fig. S26). It was found that the protonation of pyridinic N weakens the adsorption of O_2 on adjacent FeN_4 sites (fig. S27). Correspondingly, the O—O bond length is shorter than that without protonation, resulting in a higher energy barrier for the cleavage of O—O bonds and consequently a slower ORR (*44*, *45*).

Another question that needs to be answered is why Fe/N/C catalysts can still show high ORR activity under aqueous RDE tests with H_2SO_4 or $HClO_4$ as the electrolyte (fig. S28). Because pyridinic N can be rapidly protonated by small molecular acids, the Fe/N/C catalyst should quickly lose its high ORR activity (*46*). We found that the key factor is Nafion, the most frequently used binder. During the RDE test, the catalyst is first mixed with Nafion in the ink, dispersed and dried on the electrode, and immersed in aqueous solution to lastly perform the ORR. After the mixing and drying processes, Nafion coats the catalyst particles and forms a cation-selective thin film, which limits the entrance of H_2SO_4 into the micropores by blocking the anion. Therefore, high ORR activity can still be observed in the aqueous RDE test. When acid contact was carried out before coating with Nafion, 72% of the mass activity at 0.8 V_{RHE} was lost (fig. S29). Moreover, if the binder was replaced by polyvinylidene

fluoride without a cation-selective function, then rapid activity loss was observed (fig. S30). These observations support the notion that Nafion protects the micropores. Because of the heterogeneity in particle morphology, Nafion cannot completely cover the catalyst particles. However, N species on the external surface may help the Nafion to coat most of the particles via chemical interaction (*47*).

On the basis of the above results, we proposed a model for the TPB of Fe/N/C catalyst layers, as shown in Fig. 4. There are two types of TPBs: (i) Mesopores or macropores (>2.0 nm) in which acid-alkaline interactions exist at the catalyst-electrolyte interface and (ii) micropores (0.8 to 2.0 nm) without these interactions. Because the catalyst-electrolyte interaction, i.e., protonation of pyridinic N, deactivates the active sites, the mesopores or macropores contribute less than 30% to the ORR activity. In contrast, micropores (0.8 to 2.0 nm) without the protonation of pyridinic N contribute more than 70% to the ORR activity. To distinguish the two types of TPBs, we defined the former as an inactive TPB and the latter as an active TPB. In active TPBs. Nafion does not directly contact the active sites in the micropores, and proton transfer may occur via a hopping mechanism assisted by one-dimensional water chains (*48*, *49*). Furthermore, this model clarifies the mechanism of mesopores or macropores improving the ORR activity of Fe/N/C catalysts (*36*). It is not via hosting active sites with faster mass transfer but rather via exposing active sites that are secluded in micropores.

ORR needs H^+ to pass through micropores to access the active sites. An interesting question is arising: Why do H^+ cannot protonate the pyridinic N inside the micropores? Most pyridinic N species in the micropores exist as the unprotonated state after the ORR, which is confirmed by the comparison of XPS N1s species before and after five cycles of fuel cell polarization test (fig. S31). Because of large size, Nafion and the attached sulfonic anions cannot enter the micropores. If the pyridinic N species in the micropores are massively protonated without anions, then micropore environment cannot hold the electroneutrality and thus is thermodynamically unfavorable. In contrast, ORR ($O_2 + 4H^+ + 4e \rightarrow 2H_2O$) will not result in the accumulation of the net charges in the micropores so that this process can occur continuously.

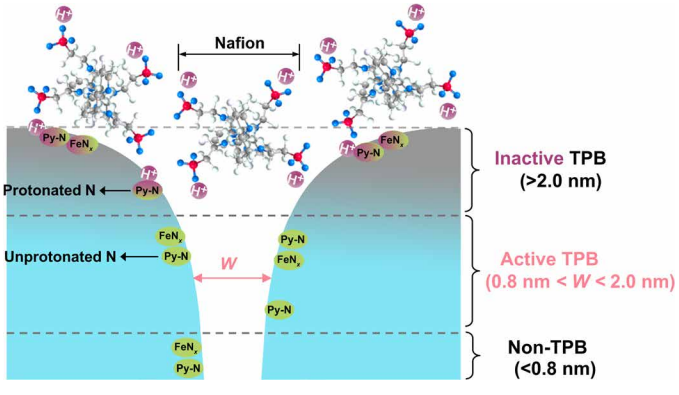

Fig. 4. Active and inactive TPBs. Acid-alkaline interaction of catalyst-electrolyte interface, i.e., protonation of pyridinic N, deactivates active sites in mesopores or macropores (>2.0 nm), forming an inactive TPB. Near-surface micropores from 0.8 to 2.0 nm, not directly contacting with Nafion, form an active TPB and contribute most of ORR activity. Micropores below 0.8 nm cannot form the TPB due to extremely slow mass transfer.

In summary, we developed a size-sensitive molecular probe method to reveal that more than 70% of the ORR activity can be attributed to micropores with sizes from 0.8 to 2.0 nm in the Fe/N/C catalyst layer of PEMFCs, regardless of the micropore surface fraction. The acid-alkaline interaction between the catalyst (pyridinic N) and electrolyte (Nafion) deactivates the active sites in mesopores or macropores, leading to an inactive TPB, although they have faster mass transfer. The absence of these interactions results in the formation of an active TPB in micropores. This study provides insight into the design and construction of advanced Pt-free ORR catalysts and catalyst layers for fuel cells.

MATERIALS AND METHODS

Chemicals

M-phenylenediamine (98.5%; Shanghai Wulian), *p*-aminobenzene sulfonic acid (98.5%; Alfa Aesar), chloroform (99%; Sinopharm), sodium hydroxide (99%; Sinopharm), sodium nitrite (99%; Sinopharm), ammonium persulfate (98.5%; Sinopharm), iron trichloride hexahydrate (99%; Sinopharm), FePc (98%; Sigma-Aldrich), dimethyl formamide (DMF; analytical reagent, AR, Sinopharm), Ketjenblank EC600J carbon black (KJ600, AkzoNobel), Ph_4Pp (99%; Macklin), $C_{10}Cl_8$ (99%; Macklin), $C_{60}Cl_{22}$ (homemade), $C_{96}Cl_{27}$ (homemade), Ph (99%; Macklin), Ph_2 (99%; Macklin), Ph_4 (99%; Macklin), sulfuric acid (96%; Sinopharm), hydrochloric acid (37%; Sinopharm), reduced iron powder (98%; Sinopharm), isopropyl alcohol (AR, Sinopharm), ethanol (AR, Sinopharm), dimethyl sulfoxide (AR, Sinopharm), acetonitrile-d_3 (99.8%; Aladdin), Nafion (20 wt%; DuPont), Nafion 212 membrane (DuPont), gas diffusion layer (3260; Ballard), and commercial Pt/C gas diffusion electrodes (0.4 mg_{Pt} cm^{-2}; Johnson Matthey, JM) are used in this study.

Synthesis of PDA-Ar Fe/N/C catalyst

The Fe/N/C-Ar catalyst was prepared through a two-step high-temperature pyrolysis method in combination with an acid leaching process, according to a previously reported method (*24*). First, 2 g of KJ600 carbon black was dispersed in 60 ml of deionized (DI) water under an ice bath condition (<3°C). In another flask, 1.418 g of *p*-aminobenzene sulfonic acid was dissolved in 60 ml of DI water under an ice bath condition, followed by successive addition of 18 ml of NaOH solution (1 mol/liter), 42 ml of HCl solution (1 mol/liter), and lastly, 8 ml of $NaNO_2$ (1 mol/liter) by dropping slowly to prepare diazonium salt. After stirring for 50 min, the as-prepared diazonium salt was poured into the carbon black solution. After stirring for 15 min, 1.396 g of iron powder was added to accelerate the surface grafting of sulfophenyl groups on KJ600 carbon black. Then, concentrated HCl (36 wt %, 50 ml), *m*-phenylenediamine (15.22 g), $(NH_4)_2S_2O_8$ (2 M, 140 ml), and $FeCl_3$ (1 M, 45 ml) were added to the slurry successively. After stirring for 17 hours, the slurry was processed by extraction filtration and washing and vacuum drying to obtain a black powder. The powder was then subjected to milling. A total of 0.6 g of the powder was dissolved in 60 ml of DI water, followed by the addition of 1.6 ml of $FeCl_3$ solution (1 mol/liter). Subsequently, the dispersed powder was dried in a rotary evaporator at 50°C. The obtained precursors were pyrolyzed under an Ar atmosphere at 950°C for 1 hour. The resulting carbonized material was subjected to acid treatment (1 M HCl, 100 ml) at 80°C for 12 hours. After centrifugation and washing, the as-prepared powder was again pyrolyzed at 950°C for 3 hours to obtain the final catalyst. The

main purpose of the first pyrolysis process was to drive the formation of Fe-N_x catalytic sites. However, some inactive Fe particles may also be formed in this process. Therefore, an acid leaching step was carried out, during which inactive or less active Fe particles exposed on the surface were removed, and those metal ions dissolved in the aqueous solution were redistributed on the catalyst surface. In the second pyrolysis process, these surface Fe sites would transform into Fe-N_x active sites to increase the density of active sites of Fe/N/C catalyst. The selection of 950°C for the pyrolysis process was because the optimal pyrolysis temperature for the active site formation was in the range of 900° to 1000°C.

Synthesis of PDA-CO_2 series Fe/N/C catalysts

The synthetic process for the PDA-CO_2 series catalysts is similar to that of the PDA-Ar catalyst, except for the replacement of Ar atmosphere by a CO_2-Ar gas mixture in the first pyrolysis process. At first, the obtained catalyst precursors were pyrolyzed under Ar/CO_2 gas mixture (CO_2 volumetric proportion was 0, 0.25, 0.75, 1.25, 2.5, 5, 7, 8.5, and 10%) at 950°C for 1 hour, followed by acid treatment (1 mol/liter HCl solution at 80°C for 12 hours), and lastly pyrolyzed for the second time in Ar at 950°C for 3 hours.

Synthesis of ZIF-Ar catalyst

The ZIF-Ar catalyst was synthesized by one-step pyrolyzing Fe-doped ZIF-8 particles under Ar atmosphere according to a previously reported method (*38*). The ZIF-8 particles were prepared as follows: 1.6 g of $Zn(NO_3)_2{\cdot}6H_2O$ and 74 mg of $FeSO_4{\cdot}7H_2O$ were dissolved in 100 ml of methanol, followed by the addition of 2-methylimidazole (3.7 g), and stirred for 24 hours at room temperature. The product was purified by centrifugation and washed thoroughly with ethanol for three times and lastly dried overnight at 80°C. The as-obtained ZIF sample was subjected to heat treatment at 1000°C under Ar atmosphere for 1 hour.

Synthesis of FePc@KJ600 catalyst

The FePc@KJ600 catalyst was synthesized by loading FePc on KJ600 carbon black. First, 0.16 g of FePc was dissolved in 100 ml of DMF, followed by the addition of 0.32 g of KJ600 carbon black. Successively, the slurry was subjected to sonication for 1 hour and stirred for 5 hours. Last, the powder product was obtained by rotary evaporation and vacuum drying for 12 hours at 90°C.

RDE test of bare sample

The ORR polarization curves of Fe/N/C catalysts were recorded on a CHI-760D biopotentistat in a standard three-electrode system with a glassy carbon (GC; φ = 5.61 mm) disk Pt ring electrode coated with Fe/N/C catalyst as the working electrode, a GC plate as the counter electrode, and the reversible hydrogen electrode (RHE) as a reference electrode. Initially, a catalyst ink was prepared. Six milligrams of Fe/N/C catalyst and 50 μl of 5 wt % Nafion were ultrasonically dispersed in 1 ml of a mixed ethanol-water solvent with a volumetric ratio of 1:1. The concentration of the catalyst in the ink is 6 mg ml^{-1}. Then, 25 μl of above ink was coated on the GC disk electrode and dried at room temperature to obtain a controlled catalyst loading of 0.6 mg cm^{-2}. Second, the as-prepared working electrode was immersed in an O_2-saturated H_2SO_4 solution (0.1 mol $liter^{-1}$) at 30°C. The CV experiment was performed by potential cycling between 0.2 and 1.0 V (RHE) at a scan rate of 10 mV s^{-1}. Then, purging gas was switched to high-purify Ar for at least 30 min to record the background current. The final ORR polarization curve was obtained by correcting the background current and compensating for the ohmic drop.

Fuel cell polarization performance test of the bare sample

The fabrication of MEA consisted of three steps: preparing the catalyst ink, coating the ink on a gas diffusion layer (GDL), and a hot-pressing process. The cathode catalyst ink was prepared by adding 10 mg of ORR catalyst (Fe/N/C or FePc@KJ600) and 280 μl of Nafion solution (5 wt %; DuPont) into 1.5 ml of ethanol. The concentration of the catalyst in the ink is 6.66 mg ml^{-1}. After ultrasonic dispersing for 1 hour (T < 10°C), the ink was coated on a GDL equipped with a microporous layer at a catalyst loading of 4 mg cm^{-2}. The MEA was fabricated by hot pressing (3 MPa) a cathode, a commercial Pt/C anode with a Pt loading of 0.4 mg cm^{-2}, and an Nafion 212 membrane (DuPont) at 135°C for 2 min. The active area of MEA was 1.21 cm^2. The weight ratio of Fe/N/C catalyst (or FePc) to Nafion was nearly 1:1.3. Polarization and durability curves were measured at 80°C on a Model 850e fuel cell test system (Scribner Associates Inc.). H_2 and O_2 loaded with 100% relative humidity (RH) were fed as fuel and oxidant, respectively, at a flow rate of 0.3 standard liters per minute (SLPM). A backpressure of 1 bar was applied.

Electrochemical molecular probe experiments in H_2-O_2 PEMFC

The molecular probe method consists of the following two processes: (i) absorption of organics by Fe/N/C catalysts and (ii) fuel cell polarization curve tests in H_2-O_2 PEMFC. First, a desired concentration of organics in the ethanol-chloroform solvent was selected. The volume ratio of ethanol to chloroform was 1:2, and the solvent volume was 1.5 ml. Afterward, 10 mg of Fe/N/C catalyst was added to the solution. The slurry was then subjected to ultrasonic dispersion for 2 hours and standing overnight at 50°C, during which organics can be fully absorbed by the catalyst. In the followed process, the solvent was not refreshed, which avoids breaking the absorption equilibrium and changing the absorption number of organics by the catalyst. Subsequently, 5 wt % Nafion solution was added to form the cathode ink. The weight ratio of Fe/N/C catalyst to Nafion was 1:1.3. The MEA fabrication and cell performance tests were the same as the bare sample. In the probe experiment, a mixed solvent was selected to dissolve the organics, which is different from that in the bare sample using the ethanol solvent. To exclude the possible influence of the solvent in the MEA preparation process, the polarization performance of the PDA-Ar cathode prepared with different solvents was compared (fig. S32). Only 7% of performance variation at 0.8 $V_{iR\text{-free}}$ was observed, excluding the impact of solvents on fuel cell performance.

Deactivation of ORR catalysts by acids in H_2-O_2 PEMFC

The deactivation experiment consists of two processes: (i) the addition of acids in the cathode ink preparation process and (ii) followed by polarization test in H_2-O_2 PEMFC. First, 2.5 or 10 μmol of H_2SO_4 (or $HClO_4$) and 10 mg of ORR catalyst (Fe/N/C or FePc@KJ600) were dispersed in 1.5 ml of ethanol, and the dispersion was stirred for 1 hour. Then, 280 μl of Nafion solution (5 wt %) was added to form the cathode ink. The MEA fabrication and cell performance tests were executed analogous to that for the bare sample.

Deactivation of ORR catalysts by acids in RDE test conditions

Acid treatment before Nafion coating

First, 6 mg of the ORR catalyst and 10 μmol of H_2SO_4 were ultrasonically dispersed in 1 ml of ethanol-water mixture with a volumetric

ratio of 1:1 for 1 hour. Then, 50 μl of 5 wt % Nafion was added. After ultrasonic dispersion for another 1 hour, 25 μl of the ink was coated on a GC disk electrode and dried at room temperature to obtain a catalyst loading of 0.6 mg cm^{-2}. The following RDE test was the same as the bare sample.

PVDF was used as binder

First, 6 mg of ORR catalyst and 0.23 mg of polyvinylidene difluoride (PVDF) were ultrasonically dispersed in 1 ml of ethanol-water solvent with a volumetric ratio of 1:1. Then, 25 μl of the ink was coated on a GC disk electrode and dried at room temperature with a catalyst loading of 0.6 mg cm^{-2}. The following RDE test was the same as the bare sample.

ORR activity recovery experiment in H_2-O_2 PEMFC

First, 10 μmol of H_2SO_4 was added into the slurry consisting of 10 mg of Fe/N/C catalyst and 1.5 ml of ethanol. After ultrasonic dispersion for 1 hour, 20 μmol of NaOH was added to neutralize the solution. Subsequently, the slurry was subjected to centrifugation, followed by washing with ethanol until the pH was close to 7. Afterward, 280 μl of Nafion solution (5 wt %) and 1.5 ml of ethanol were added to prepare the cathode ink. The following MEA fabrication and cell performance test were the same as stated before.

Absorption capacity test

The amount of organics absorbed to the Fe/N/C catalysts was determined by measuring the concentration of organics in the solution before and after the absorption process via ultraviolet-visible (UV-Vis) spectrophotometry. The absorption process was the same as the probe experiment. In detail, a desired concentration of organics in 1.5 ml of ethanol-chloroform solvent was selected. The volume ratio of ethanol to chloroform was 1:2. Afterward, 10 mg of Fe/N/C catalyst was added to the solution. The slurry was subjected to ultrasonic dispersion for 2 hours and standing overnight at 50°C. The supernatant liquor was obtained by centrifugation and pipetted for consequent concentration test. The concentration of organics in the solution before and after the absorption was analyzed by UV-Vis spectroscopy. The test process was as follows: The test sample was diluted by a factor of 1 to 600 times (Ph, 1 time; Ph_2, 25 times; Ph_4, 200 times; $C_{10}Cl_8$, 200 times; Ph_4Pp, 600 times, C60Cl22, 300 times, and C_{96} Cl_{27}, 100 times). Then, the absorption spectra from 600 to 200 nm were measured with the Varian Cary 5000 spectrometer. Pure solvents were measured beforehand as reference (blank). The concentration of organics was determined by an external reference method.

Isothermal absorption/desorption test

The change of micropore accessibility was examined by measuring the Ar isothermal adsorption/desorption curves of Fe/N/C catalysts after the organics were applied to the catalyst surface but before the catalyst was fabricated into the MEA. The absorption process was the same as the probe experiment. In detail, a desired concentration of organics in 7.5 ml of ethanol-chloroform solvent was selected. The volume ratio of ethanol to chloroform was 1:2. Afterward, 50 mg of Fe/N/C catalyst was added to the solution. The slurry was subjected to ultrasonic dispersion for 2 hours and standing overnight at 50°C. Then, the solvents were removed via centrifugation and vacuum drying at 40°C overnight. The as-obtained catalysts were then subjected to the Ar isothermal adsorption/desorption test. The degassing condition was 80°C at vacuum for 10 hours. The reference data were obtained by measuring the catalyst that went through the same treatment process but without the organics.

Acid-alkaline titration experiment

First, 12 pieces of aqueous solution (10 ml) with a given pH (ranging from 1 to 12) were prepared. The pH of the solutions was adjusted by addition of 0.1 M H_2SO_4 or 0.1 M NaOH aqueous solution. Twenty milligrams of PDA-Ar catalyst was then added into the above 12 different solutions. Each sample was left for equilibration for 10 hours. Last, the pH value of resultant aqueous solution was measured.

Physical characterizations

XPS (Qtac 100 LEISS-XPS instrument) was performed to characterize the surface composition of Fe/N/C catalysts. The Ar absorption/desorption isotherm was measured with an ASAP 2020 physisorption analyzer (Micromeritics). Micropore size distribution was obtained by the Horvath-Kawazoe method, and the mesopore size distribution was obtained by the Barrett-Joyner-Halenda method. The absorption branch data were used. UV-Vis spectroscopy was performed with a Varian Cary 5000 spectrophotometer to quantify the concentration of organics before and after the absorption experiments. The content of Fe element in the samples is determined by the ICP-MS (PerkinElmer, NexION 300). Extended x-ray absorption fine structure data of Fe *K*-edge were acquired at the Beijing Synchrotron Radiation Facility (1W1B) in fluorescence mode. The incident x-rays were monochromatized using Si (111) double crystals. The raw data were processed and fitted by the standard procedures with Athena and Artemis programs. The x-ray absorption near-edge structure fitting was processed using the MXAN package. A 27-W black light lamp (FPL27BLB, Sankyo Denki, Japan) was added between the gamma-ray detector and the catalyst sample holder to perform Mössbauer measurements under UV irradiation. The spectra were fitted with the appropriate superpositions of Lorentzian lines using the MossWinn 3.0i computer program.

Computational methods

Calculation of O2 adsorption energy and O—O bond length

All spin-polarized computations were performed by ORCA in this work (*50*). The Def2-TZVP basis set combined with the resolution of identity (RI) approximation was applied (*51*). All molecular structures were studied with the Perdew-Burke-Ernzerhof function in combination with the dispersion correction (*52*–*54*). The dipole correction was included for all the computations. For the FeN_4 molecular structures with the protonated pyridine N, the net charge was set to be 1. The O_2 adsorption energy was calculated according to the following equation

$$E_{ads} = E_{molecule-O_2} - E_{molecule} - E_{O_2}$$

where $E_{molecule-O2}$, $E_{molecule}$, and E_{O2} were the total energy of the molecule with O_2 adsorption, the molecule, and the O_2 in gas phase, respectively.

Calculation of dynamic diameter

The organic molecules were optimized on the same theory level with the computation of O_2 adsorption. The optimized geometry of the organic molecules was measured in terms of length, width, and height by placing them completely into the smallest cuboid box.

The cross-sectional area of the box in the horizontal plane was chosen because it showed the largest area (*55*). The molecules were approximated to be in a circular shape, and the dynamic diameter of the molecule was calculated according to the following equation

$$d = 2^{*}\sqrt{\frac{A}{3.1412}}$$

where d and A were the dynamic diameter and the cross-sectional area in the horizontal plane, respectively.

SUPPLEMENTARY MATERIALS

Supplementary material for this article is available at https://science.org/doi/10.1126/sciadv.add8873

REFERENCES AND NOTES

1. M. Lefevre, E. Proietti, F. Jaouen, J. P. Dodelet, Iron-based catalysts with improved oxygen reduction activity in polymer electrolyte fuel cells. *Science* **324**, 71–74 (2009).
2. G. Wu, K. L. More, C. M. Johnston, P. Zelenay, High-performance electrocatalysts for oxygen reduction derived from polyaniline, iron, and cobalt. *Science* **332**, 443–447 (2011).
3. D. Guo, R. Shibuya, C. Akiba, S. Saji, T. Kondo, J. Nakamura, Active sites of nitrogen-doped carbon materials for oxygen reduction reaction clarified using model catalysts. *Science* **351**, 361–365 (2016).
4. H. T. Chung, D. A. Cullen, D. Higgins, B. T. Sneed, E. F. Holby, K. L. More, P. Zelenay, Direct atomic-level insight into the active sites of a high-performance PGM-free ORR catalyst. *Science* **357**, 479–484 (2017).
5. A. Zitolo, V. Goellner, V. Armel, M. T. Sougrati, T. Mineva, L. Stievano, E. Fonda, F. Jaouen, Identification of catalytic sites for oxygen reduction in iron- and nitrogen-doped graphene materials. *Nat. Mater.* **14**, 937–942 (2015).
6. H. Zhang, H. T. Chung, D. A. Cullen, S. Wagner, U. I. Kramm, K. L. More, P. Zelenay, G. Wu, High-performance fuel cell cathodes exclusively containing atomically dispersed iron active sites. *Energ. Environ. Sci.* **12**, 2548–2558 (2019).
7. D. Liu, J. C. Li, S. Ding, Z. Lyu, S. Feng, H. Tian, C. Huyan, M. Xu, T. Li, D. Du, P. Liu, M. Shao, Y. Lin, 2D single-atom catalyst with optimized iron sites produced by thermal melting of metal-organic frameworks for oxygen reduction reaction. *Small Methods* **4**, 1900827 (2020).
8. F. Jaouen, V. Goellner, M. Lefèvre, J. Herranz, E. Proietti, J. P. Dodelet, Oxygen reduction activities compared in rotating-disk electrode and proton exchange membrane fuel cells for highly active Fe-N-C catalysts. *Electrochim. Acta* **87**, 619–628 (2013).
9. J. Fan, M. Chen, Z. Zhao, Z. Zhang, S. Ye, S. Xu, H. Wang, H. Li, Bridging the gap between highly active oxygen reduction reaction catalysts and effective catalyst layers for proton exchange membrane fuel cells. *Nat. Energy* **6**, 475–486 (2021).
10. D. Banham, S. Ye, Current status and future development of catalyst materials and catalyst layers for proton exchange membrane fuel cells: An industrial perspective. *ACS Energy Lett.* **2**, 629–638 (2017).
11. Y. Guo, F. Pan, W. Chen, Z. Ding, D. Yang, B. Li, P. Ming, C. Zhang, The controllable design of catalyst inks to enhance PEMFC performance: A review. *Electrochem. Energy Rev.* **4**, 67–100 (2020).
12. P. Choi, N. H. Jalani, R. Datta, Thermodynamics and proton transport in nafion. *J. Electrochem. Soc.* **152**, E123 (2005).
13. K. A. Mauritz, R. B. Moore, State of understanding of Nafion. *Chem. Rev.* **104**, 4535–4586 (2004).
14. Q. Meyer, J. Hack, N. Mansor, F. Iacoviello, J. J. Bailey, P. R. Shearing, D. J. L. Brett, Multi-scale imaging of polymer electrolyte fuel cells using x-ray micro- and nano-computed tomography, transmission electron microscopy and helium-ion microscopy. *Fuel Cells* **19**, 35–42 (2019).
15. S. Komini Babu, H. T. Chung, P. Zelenay, S. Litster, Resolving electrode morphology's impact on platinum group metal-free cathode performance using nano-CT of 3D hierarchical pore and ionomer distribution. *ACS Appl. Mater. Interfaces* **8**, 32764–32777 (2016).
16. I. Martens, A. Vamvakeros, N. Martinez, R. Chattot, J. Pusa, M. V. Blanco, E. A. Fisher, T. Asset, S. Escribano, F. Micoud, T. Starr, A. Coelho, V. Honkimaki, D. Bizzotto, D. P. Wilkinson, S. D. M. Jacques, F. Maillard, L. Dubau, S. Lyonnard, A. Morin, J. Drnec, Imaging heterogeneous electrocatalyst stability and decoupling degradation mechanisms in operating hydrogen fuel cells. *ACS Energy Lett.* **6**, 2742–2749 (2021).
17. M. Tesfaye, A. N. MacDonald, P. J. Dudenas, A. Kusoglu, A. Z. Weber, Exploring substrate/ionomer interaction under oxidizing and reducing environments. *Electrochem. Commun.* **87**, 86–90 (2018).
18. S. Chiriaev, N. Dam Madsen, H.-G. Rubahn, S. Ma Andersen, Helium ion microscopy of proton exchange membrane fuel cell electrode structures. *AIMS Mater. Sci.* **4**, 1289–1304 (2017).
19. T. Terao, G. Inoue, M. Kawase, N. Kubo, M. Yamaguchi, K. Yokoyama, T. Tokunaga, K. Shinohara, Y. Hara, T. Hara, Development of novel three-dimensional reconstruction method for porous media for polymer electrolyte fuel cells using focused ion beam-scanning electron microscope tomography. *J. Power Sources* **347**, 108–113 (2017).
20. F. Yang, L. Xin, A. Uzunoglu, Y. Qiu, L. Stanciu, J. Ilaysky, W. Li, J. Xie, Investigation of the interaction between nafion ionomer and surface functionalized carbon black using both ultrasmall angle x-ray scattering and cryo-TEM. *ACS Appl. Mater. Interfaces* **9**, 6530–6538 (2017).
21. H. Kang, S. H. Kwon, R. Lawler, J. H. Lee, G. Doo, H.-T. Kim, S.-D. Yim, S. S. Jang, S. G. Lee, Nanostructures of nafion film at platinum/carbon surface in catalyst layer of PEMFC: Molecular dynamics simulation approach. *J. Phys. Chem. C* **124**, 21386–21395 (2020).
22. Q. Meyer, Y. Zeng, C. Zhao, In situ and operando characterization of proton exchange membrane fuel cells. *Adv. Mater.* **31**, e1901900 (2019).
23. M. Rauf, Y.-D. Zhao, Y.-C. Wang, Y.-P. Zheng, C. Chen, X.-D. Yang, Z.-Y. Zhou, S.-G. Sun, Insight into the different ORR catalytic activity of Fe/N/C between acidic and alkaline media: Protonation of pyridinic nitrogen. *Electrochem. Commun.* **73**, 71–74 (2016).
24. Q. Wang, Z. Y. Zhou, Y. J. Lai, Y. You, J. G. Liu, X. L. Wu, E. Terefe, C. Chen, L. Song, M. Rauf, N. Tian, S. G. Sun, Phenylenediamine-based $FeN_{(x)}$/C catalyst with high activity for oxygen reduction in acid medium and its active-site probing. *J. Am. Chem. Soc.* **136**, 10882–10885 (2014).
25. V. Yarlagadda, M. K. Carpenter, T. E. Moylan, R. S. Kukreja, R. Koestner, W. Gu, L. Thompson, A. Kongkanand, Boosting fuel cell performance with accessible carbon mesopores. *ACS Energy Lett.* **3**, 618–621 (2018).
26. E. Antolini, Carbon supports for low-temperature fuel cell catalysts. *Appl. Catal. B Environ.* **88**, 1–24 (2009).
27. Y. C. Wang, Y. J. Lai, L. Song, Z. Y. Zhou, J. G. Liu, Q. Wang, X. D. Yang, C. Chen, W. Shi, Y. P. Zheng, M. Rauf, S. G. Sun, S-doping of an Fe/N/C ORR catalyst for polymer electrolyte membrane fuel cells with high power density. *Angew. Chem. Int. Ed.* **54**, 9907–9910 (2015).
28. Y. Li, P. Zhang, L. Wan, Y. Zheng, X. Qu, H. Zhang, Y. Wang, K. Zaghib, J. Yuan, S. Sun, Y. Wang, Z. Zhou, S. Sun, A general carboxylate-assisted approach to boost the ORR performance of ZIF-derived Fe/N/C catalysts for proton exchange membrane fuel cells. *Adv. Funct. Mater.* **31**, 2009645 (2021).
29. X. Fu, P. Zamani, J. Y. Choi, F. M. Hassan, G. Jiang, D. C. Higgins, Y. Zhang, M. A. Hoque, Z. Chen, In situ polymer graphenization ingrained with nanoporosity in a nitrogenous electrocatalyst boosting the performance of polymer-electrolyte-membrane fuel cells. *Adv. Mater.* **29**, 1604456 (2017).
30. Q. Liu, X. Liu, L. Zheng, J. Shui, The solid-phase synthesis of an Fe-N-C electrocatalyst for high-power proton-exchange membrane fuel cells. *Angew. Chem. Int. Ed.* **57**, 1204–1208 (2018).
31. Y.-C. Wang, Y.-J. Lai, L.-Y. Wan, H. Yang, J. Dong, L. Huang, C. Chen, M. Rauf, Z.-Y. Zhou, S.-G. Sun, Suppression effect of small organic molecules on oxygen reduction activity of Fe/N/C catalysts. *ACS Energy Lett.* **3**, 1396–1401 (2018).
32. A. P. Young, J. Stumper, S. Knights, E. Gyengea, Ionomer degradation in polymer electrolyte membrane fuel cells. *J. Electrochem. Soc.* **157**, B425–B436 (2010).
33. R. Makharia, M. F. Mathias, D. R. Bakerb, Measurement of catalyst layer electrolyte resistance in PEFCs using electrochemical impedance spectroscopy. *J. Electrochem. Soc.* **152**, A970–A977 (2005).
34. L. Wan, W. Chen, H. Xu, Y. Wang, J. Yuan, Z. Zhou, S. Sun, A mild CO_2 etching method to tailor the pore structure of platinum-free oxygen reduction catalysts in proton exchange membrane fuel cells. *ACS Appl. Mater. Interfaces* **13**, 45661–45669 (2021).
35. L. Yang, X. Zeng, W. Wang, D. Cao, Recent progress in MOF-derived, heteroatom-doped porous carbons as highly efficient electrocatalysts for oxygen reduction reaction in fuel cells. *Adv. Funct. Mater.* **28**, 1704537 (2018).
36. X. Wan, X. Liu, Y. Li, R. Yu, L. Zheng, W. Yan, H. Wang, M. Xu, J. Shui, Fe–N–C electrocatalyst with dense active sites and efficient mass transport for high-performance proton exchange membrane fuel cells. *Nat. Catal.* **2**, 259–268 (2019).
37. E. Proietti, F. Jaouen, M. Lefevre, N. Larouche, J. Tian, J. Herranz, J. P. Dodelet, Iron-based cathode catalyst with enhanced power density in polymer electrolyte membrane fuel cells. *Nat. Commun.* **2**, 416 (2011).
38. C. Zhang, Y.-C. Wang, B. An, R. Huang, C. Wang, Z. Zhou, W. Lin, Networking pyrolyzed zeolitic imidazolate frameworks by carbon nanotubes improves conductivity and enhances oxygen-reduction performance in polymer-electrolyte-membrane fuel cells. *Adv. Mater.* **29**, 1604556 (2016).
39. S. H. Lee, J. Kim, D. Y. Chung, J. M. Yoo, H. S. Lee, M. J. Kim, B. S. Mun, S. G. Kwon, Y. E. Sung, T. Hyeon, Design principle of Fe-N-C electrocatalysts: How to optimize multimodal porous structures? *J. Am. Chem. Soc.* **141**, 2035–2045 (2019).
40. C. Welch, A. Labouriau, R. Hjelm, B. Orler, C. Johnston, Y. S. Kim, Nafion in dilute solvent systems: Dispersion or solution? *ACS Macro Lett.* **1**, 1403–1407 (2012).

41. S. Men, D. S. Mitchell, K. R. Lovelock, P. Licence, X-ray photoelectron spectroscopy of pyridinium-based ionic liquids: Comparison to imidazolium- and pyrrolidinium-based analogues. *ChemPhysChem* **16**, 2211–2218 (2015).
42. G. Liu, X. G. Li, P. Ganesan, B. N. Popov, Studies of oxygen reduction reaction active sites and stability of nitrogen-modified carbon composite catalysts for PEM fuel cells. *Electrochim. Acta* **55**, 2853–2858 (2010).
43. J. Herranz, F. Jaouen, M. Lefevre, U. I. Kramm, E. Proietti, J. P. Dodelet, P. Bogdanoff, S. Fiechter, I. Abs-Wurmbach, P. Bertrand, T. M. Arruda, S. Mukerjee, Unveiling N-protonation and anion-binding effects on Fe/N/C catalysts for O_2 reduction in proton-exchange-membrane fuel cells. *J. Phys. Chem. C* **115**, 16087–16097 (2011).
44. R. Ma, G. Lin, Q. Ju, W. Tang, G. Chen, Z. Chen, Q. Liu, M. Yang, Y. Lu, J. Wang, Edge-sited Fe-N_4 atomic species improve oxygen reduction activity via boosting O_2 dissociation. *Appl. Catal. B-Environ* **265**, 118593 (2020).
45. A. Omidvar, Dissociation of O_2 molecule on Fe/Nx clusters embedded in C60 fullerene, carbon nanotube and graphene. *Synthetic Met.* **234**, 38–46 (2017).
46. D. Banham, S. Ye, K. Pei, J.-i. Ozaki, T. Kishimoto, Y. Imashiro, A review of the stability and durability of non-precious metal catalysts for the oxygen reduction reaction in proton exchange membrane fuel cells. *J. Power Sources* **285**, 334–348 (2015).
47. S. Ott, A. Orfanidi, H. Schmies, B. Anke, N. Hong Nhan, J. Huebner, U. Gernert, M. Gliech, M. Lerch, P. Strasser, Ionomer distribution control in porous carbon-supported catalyst layers for high-power and low Pt-loaded proton exchange membrane fuel cells. *Nat. Mater.* **19**, 77–85 (2020).
48. R. H. Tunuguntla, F. I. Allen, K. Kim, A. Belliveau, A. Noy, Ultrafast proton transport in sub-1-nm diameter carbon nanotube porins. *Nat. Nanotechnol.* **11**, 639–644 (2016).
49. Z. Cao, Y. X. Peng, T. Y. Yan, S. Li, A. L. Li, G. A. Voth, Mechanism of fast proton transport along one-dimensional water chains confined in carbon nanotubes. *J. Am. Chem. Soc.* **132**, 11395–11397 (2010).
50. F. Neese, The ORCA program system. *WIREs Comput. Mol. Sci.* **2**, 73–78 (2012).
51. F. Weigend, R. Ahlrichs, Balanced basis sets of split valence, triple zeta valence and quadruple zeta valence quality for H to Rn: Design and assessment of accuracy. *Phys. Chem. Chem. Phys.* **7**, 3297–3305 (2005).
52. J. P. Perdew, K. Burke, M. Ernzerhof, Generalized gradient approximation made simple. *Phys. Rev. Lett.* **77**, 3865–3868 (1996).
53. S. Grimme, J. Antony, S. Ehrlich, H. Krieg, A consistent and accurate ab initio parametrization of density functional dispersion correction (DFT-D) for the 94 elements H-Pu. *J. Chem. Phys.* **132**, 154104 (2010).
54. S. Grimme, S. Ehrlich, L. Goerigk, Effect of the damping function in dispersion corrected density functional theory. *J. Comput. Chem.* **32**, 1456–1465 (2011).
55. A. S. Sharipov, B. I. Loukhovitski, C.-J. Tsai, A. M. Starik, Theoretical evaluation of diffusion coefficients of $(Al_2O_3)n$ clusters in different bath gases. *Eur. Phys. J. D* **68**, 1–9 (2014).

Acknowledgments: We acknowledge the staff of the Beijing Synchrotron Radiation Facility (1W1B, BSRF) for the support in XAS measurements. We thank G.-X. Zhang for the modifications to the manuscript. **Funding:** This work was supported by the National Key Research and Development Program of China (2021YFA1501504), National Natural Science Foundation of China (22179116, 92045302, and 22021001), and Fundamental Research Funds for the Central Universities (20720220017). **Author contributions:** Y.-C.W., S.-H.S. and Z.-Y.Z. designed the experiments. Y.-C.W., W.H., and L.-Y.W. performed the majority of synthesis, characterization, and electrochemical tests. J.Y. conducted the theoretical calculation. Y.-P.Z. performed the XPS experiment. R.-J.X. and Y.-Z.T. synthesized the perchloro-organic probe molecules. L.-R.Z. analyzed the XAS data. Y.-S.W. and K.Z. modified the manuscript. S.-G.S. supervised the research. **Competing interests:** The authors declare that they have no competing interests. **Data and materials availability:** All data needed to evaluate the conclusions in the paper are present in the paper and/or the Supplementary Materials.

Submitted 16 July 2022
Accepted 15 September 2022
Published 2 November 2022
10.1126/sciadv.add8873